An experimentally based thermo-kinetic hardening model for high power direct diode laser cladding

Soundarapandian Santhanakrishnan, Fanrong Kong, Radovan Kovacevic*

Research Center for Advanced Manufacturing, Southern Methodist University, Dallas, TX, USA

ABSTRACT

High power direct diode laser (HPDDL) based cladding is found to be an economical process for repairing or building valued components and tools that are used in the automotive, aerospace, nuclear and defense industries. In this study, a 2-kW HPDDL of 808 nm in wavelength, rectangular-shaped laser spot of 12 mm × 1 mm with uniform distribution (top-hat) of laser power is used to carry out the experiments. An off-axis powder injection system is used to deposit tool steel H13 on the AISI 4140 steel substrate. A number of experiments are carried out by changing the laser power and scanning speeds while keeping a constant powder feed rate to produce different sizes of clad. An experimentally based finite element (FE) thermal model is developed to predict the cross-sectional temperature history of the cladding process. The temperature-dependent material properties and phase change kinetics are taken into account in this model. As-used experimental boundary conditions are adopted in this model. The acquired temperature history from the FE model is used to predict the temperature gradient, rates of heating and cooling cycles, and the solidification of the clad to the substrate. The FE thermal model results are coupled with thermo-kinetic (TK) equations to predict the hardness of the clad to the substrate. Metallurgical characterization and hardness measurements are performed to quantify the effect of processing parameters on the variation of clad geometry, microstructure, and the change of hardness of the clad to the substrate. The results show that a good metallurgically bonded clad of hardness uniformity is achieved.

© 2011 Elsevier B.V. All rights reserved.

1. Introduction

For a number of years, lasers have been used in the materials processing industry in broader applications such as heat treatment, melting, alloying, and cladding. However, today the one-step cladding by using a high power direct diode laser (HPDDL) compared to a CO_2 or a Nd:YAG laser is found to be a cost-effective process. The HPDDL-based cladding is used in the automotive, aerospace, nuclear, and defense industries to repair or build the valued components and tools. Kinkade (2006) briefly reported the advantages of HPDDL compared to other high power lasers (CO_2, Nd:YAG), related to its application for laser cladding. A focused laser beam with a rectangular spot (12 mm × 1 mm) and a shorter wavelength (808 nm) has better absorption by metals than CO_2 or Nd:YAG lasers. A higher wall-plug efficiency (∼30%) makes this type of laser more economical. A more uniform distribution (top-hat) of laser power across the length of the laser spot (12 mm) provides more uniform cladding with a small heat-affected zone (HAZ).

In the laser cladding process, the same or different chemical composition of clad material with respect to the substrate is used to produce a new component or a good metallurgical bond structure on the existing component. During the cladding process, a high power laser is used to melt the blown or preplaced powder particles or wire-feed at the substrate. Cook et al. (2000) demonstrated that a denser microstructure laser clad with stable bond to the substrate is generated at the high temperature. The metallurgically transformed clad structure on the valued components' enhances/improves the surface properties such as wear-resistant, corrosion-resistant, and heat-resistant.

Several methods are used to achieve a thin layer of clad in the laser cladding process, such as (1) injecting the powder particles into the molten pool generated by the high power density laser beam; (2) feeding the wire into the focal spot of the laser beam; and (3) a thin layer of powder is pre-placed on the substrate in order to expose it to the high density laser beam. In the past, the laser cladding process by powder injection has proved to produce uniform, defect-free, and a good metallurgically bonded clad on the substrate. Syed et al. (2005) studied the influence of the powder feeding direction (front side and rear side) with respect to the laser scanning direction. The angle and position of the powder feeding nozzle greatly affect the clad geometry. A small variation in the powder feed rate could significantly generate larger variations in

* Corresponding author at: Research Center for Advanced Manufacturing and Center for Laser Aided Manufacturing, Southern Methodist University, 3101 Dyer Street, Dallas, TX 75205, USA. Tel.: +1 214 768 4865; fax: +1 214 768 0812.
E-mail address: kovacevi@lyle.smu.edu (R. Kovacevic).

the geometrical features and microstructure of the clad. The "front" feeding direction was found to produce a smooth, uniform, and a good metallurgically bonded clad. In addition, a dense, crack-free, non-porous cladding, and a small HAZ were achieved.

In the laser cladding process, a strong coupling between the laser beam, powder particles, and the molten pool occurs. A larger fraction of the laser power reaches the substrate, while a smaller fraction of laser power is captured by the powder particles that will heat it up. The laser power attenuated by the powder particles and the related fluctuation of laser energy apparently changes the shape of the molten pool. The variation of molten pool shape has a significant impact of the workpiece absorption with respect to the laser beam. A number of processing parameters such as laser power, scanning speed, powder feed rate, laser focal spot, and thermo-physical properties of the materials are involved in the laser cladding process to achieve the desired clad geometry (height and width) and the surface properties. The temperature generated in the cladding process is the function of processing parameters such as laser power, scanning speed, beam angle with respect to the substrate, and the absorptivity of the clad material and the substrate to the laser beam. The clad geometry, the dilution of the clad material to the substrate, and the HAZ generated in the cladding process are the function of the thermo-physical properties of the clad material and the substrate, temperature, and time. The microstructure evolution and the corresponding mechanical and surface properties produced in the cladding process are dependent on the rates of heating and cooling cycles, temperature gradient, and the subsequent rate of solidification.

The tool steel H13 was used as a clad material in the past to build complex-shaped components employing CO_2 or a Nd:YAG laser as a heat source. Mazumdar et al. (1997) reviewed the state-of-the-art of the direct metal deposition (DMD) process. They studied the effect of the post heat treatment process on the formation of tempered microstructure, variation of hardness, and the residual stress of the multi-layer clad of tool steel H13 on the substrate of the same material using a CO_2 laser. Choi and Hua (2004) used the Taguchi Method (TM) to design the experiments of CO_2 laser cladding of H13 on the substrate of AISI 1018. The study was performed to quantify the effect of laser powder deposition (LPD) process parameters such as laser power, scanning speed, and powder flow rate on the variation of clad geometry, microstructure, change of hardness, and porosity formation. A closed-loop feedback signal acquired from the charged coupled device (CCD) camera closely monitored the variation of molten pool geometry in real time was used. From the real time image of the molten pool geometry, the powder feed rate was regulated to update the multi-layer deposition height, geometry and its surface properties. Lee et al. (2009) used a fiber laser melting to improve the surface hardness and wear-resistant of tool steel H13. They studied the effect of laser power, laser spot size, pulse frequency, and the scanning speeds on the variation of microstructure, and the change in hardness. Chiang and Chen (2005) developed a mathematical model using a modified Asby-Easterling heat transfer equation to predict the temperature history of the CO_2 laser melting of tool steel H13. The model was experimentally verified to quantify the effect of laser power, laser spot size, and the scanning speed on the variation of microstructure and phase transformations.

Recently, in SMU's Research Center for Advanced Manufacturing (RCAM), an extensive research work on the LPD process was carried out to develop new erosion-resistance materials using a Nd:YAG laser. The erosion-resistant materials are tool steel H13, or composites of WC/H13, and TiC/H13 on the substrates of AISI 4140, and AISI 1018 to build a friction stir welding (FSW) tool for extending the die casting die's service life. A functionally graded material (FGM) matrix is widely used in industry to build complex-shaped components because of their ability to withstand a huge abrasive and corrosive working environment. Ouyang et al. (2002) built a FSW tool using the FGM matrix of WC/H13, and the authors experimentally showed that the obtained FGM provided good wear-resistant at an elevated temperature. Jiang and Kovacevic (2007) studied the effect of laser scanning speed on the variation of microstructure of FGM (TiC/H13) to determine an optimal composite proportion of TiC with respect to H13 in order to achieve the desired hardness and erosion resistance. Foroozmer et al. (2009) investigated the effect of vibration on the mitigation of defects such as a lack of fusion or unmeleted particles present in the interface zone and the formation of gas porosity during the LPD process. Their experimental study demonstrated that a more uniform hardness distribution across the build-up made of tool steel H13 on the substrate of AISI 4140 was achieved, resulting in a homogeneous microstructure with an aid of vibration.

Nowadays, HPDDL is successfully used in industry as a versatile heat source for the cladding process. Abe et al. (2004) demonstrated a cladding of TiO_2–ZrO_2–WC on copper substrate that achieved a higher value of hardness (1400 $HV_{0.05}$). They reported that the laser cladding by powder injection exhibits a more uniform depth of clad with high bond strength to the substrate. Adak et al. (2005) obtained a defect-free and completely solidified cladding of Cu–30Ni alloy on the same material substrate. Lawrence (2006) repaired the damaged aircraft skin with the composite patches of polyetheretherketone (PEEK) by using an HPDL. A PEEK of 0.2 mm thickness of clad was placed on the aircraft skin (Alclad 2024 T) to increase its specific strength, stiffness, fatigue, and corrosion resistance. Bonek and Dobrzanski (2006) demonstrated that a 0.11 mm thickness of WC cladding on hot-work tool steel (X40CrMoV5) was achieved to increase its wear resistance and heat resistance. Nowotny et al. (1998) developed a fairly maximum clad height of 1.2 mm of stellite-6 on mild steel substrate. A feasibility study of HPDDL cladding compared to CO_2 laser cladding was done. A high cladding rate of 0.5 kg/h was achieved in the HPDDL cladding due to operating in a shorter wavelength (940 nm) that increased the coupling efficiency of 2.5 times more than CO_2 laser cladding. Uenishi et al. (2007) studied the effect of irradiation of CO_2 and diode lasers on the variation of microstructure, change of hardness, and the wear resistance of clad of Fe–Cr–C–Cu alloy on the substrate of Al 5052. A maximum thickness of 3 mm clad of Fe–Cr–C–Cu alloy with a minimum dilution of clad to the substrate of Al 5052 was achieved in low heat input of HPDDL compared to the high heat input of CO_2 laser.

Several numerical models were developed for laser cladding of the co-axially powder deposition process to predict the molten pool shape, dilution of the deposited material to the substrate, and the clad geometry. Fathi et al. (2006) proposed a three-dimensional (3-D) analytical model incorporating the effects of Marangoni forces and phase change kinetics to predict the melt pool shape, temperature distribution, dilution of the clad material to the substrate, and the clad geometry. Han et al. (2004) developed a mathematical model that takes into account the effects of laser–powder–substrate interactions, phase change kinetics, and the Marangoni forces on the melt pool to study the variation of fluid flow, heat transfer, and the clad geometry of the LPD process. A level set algorithm was used to study the influence of powder injection on the variation of melt pool shape, dilution of the clad material to the substrate, and the fluid flow pattern. Huang et al. (2006) presented an analytical model using the coupled Lambert–Beer theorem, Mie's theory, and the heat equilibrium principle to calculate the attenuation of laser energy by the heating of powder particles for different conditions of powder feed rate and the angle of powder feeding. The results showed that the temperature and the laser intensity distributions vary from the Gaussian distribution to an even distribution at the center of the laser beam when the powder

feed rate and the angle of powder feeding changes from the lower level to the higher level.

Picasso et al. (1994) developed an inverse process model based on the energy balance equation incorporating the effects of laser–powder–substrate. The model was used to predict the powder feed rate, scanning speed, and variation of melt pool shape for a given laser power, laser beam geometry, clad height, powder feeding nozzle geometry, size and velocity of the powder particles, and the size of overlap for the multi-track LPD process. Pinkerton and Li (2004) developed a 3-D mathematical model based on the energy and mass balances to predict the variation of clad geometry on the effect of laser power and the scanning speed for a constant powder feed rate. In this model, a single-track multi-layer clad profile was modeled by using the top layer with a circular deposition rather than a flat or elliptical profile during the LPD process. A varying scanning speed was introduced to update the molten pool geometry in order to achieve the desired clad geometry. Costa et al. (2005) developed a coupled thermo-kinetic (TK) model to calculate the final hardness of the deposited material. The temperature history and hardness results of this model showed a strong correlation between the successive layers idle time and the size of substrate. Recently, Foroozmer and Kovacevic (2009) developed a TK phase transformation model for laser cladding of the co-axially powder deposition process to study the influence of deposition patterns with respect to the change in hardness. Different deposition patterns such as long-bead, short-bead, spiral-in, and spiral-out were used to determine their effect on the variation of microstructure and the change of hardness. The authors found that the deposition pattern has a significant influence on the temperature history, phase transformations, and hardness of the LPD process.

Capello et al. (2007) developed a FE thermal model using a HPDDL for the surface treatment of welded duplex stainless steels. In this model, a rectangular laser spot was used to irradiate a constant power of laser with the natural convective cooling on top and bottom surfaces. Woo and Cho (1999) presented a 3-D analytical model incorporating the forced and natural convections at the top and bottom surfaces, respectively. The model used a CO_2 laser of rectangular beam spot to predict the temperature history, heat treated geometry, and the heat treated depth of material. The change of absorptivity of the laser beam was experimentally measured. Kasatkin and Vinokur (1984) constructed the empirical relationships to calculate the A_{C1} and A_{C3} temperatures of steels. In this model, the non-additive nature of the alloying elements and the elements interactions with respect to each other are considered. Hojerslev (2001) experimentally evaluated and reported the martensite starting (M_S) and final (M_F) temperatures of tool steels. Li et al. (1998) presented a computation model to predict the phase transformations, variation of microstructure, decomposed phases of austenite, and the change of hardness of heat treatable steels. Reti et al. (1987) developed a mathematical model to predict the transformation kinetics in steel for non-isothermal processes. The model incorporated the kinetic functions, such as temperature, time, and the activation energy.

A few numerical models are reported for laser cladding of an off-axis powder deposition process. Those models are developed for a two-dimensional (2-D) environment (Nash et al., 2004) without incorporating the effect of phase transformations (Wen and Shin, 2009). Nash et al. (2004) developed a 2-D numerical model to predict the temperature history of the LPD process. The variation of absorptivity of the laser beam with respect to change in processing parameters and the materials surface conditions was evaluated both with and without wire-feeding. Recently, Wen and Shin (2009) used the classical continuum approach to model the powder flow pattern, temperature distribution, and the clad geometry for an off-axis LPD process. To date, no TK model has been developed to predict the microstructure based on the rate of solidi-

fication and the corresponding hardness for an off-axis LPD process. Therefore, the objective of this work is to develop a TK-based hardening model for an off-axis powder deposition process using an HPDDL. The model predicts the change of hardness of the clad to the substrate. In this study, an experimentally based FE thermal model is developed to predict the cross-sectional temperature history of the laser cladding process. The acquired temperature history from the FE thermal model is coupled with TK equations to predict the variation of microstructure and the change of hardness of the clad to the substrate. Metallurgical characterization and hardness measurements are performed to quantify the effect of processing parameters on the variation of clad geometry, microstructure and the change of hardness of the clad to the substrate.

2. Experimental setup and procedures

In this study, AISI 4140 steel is chosen as a substrate. Tool steel H13 in a powder form at an average size of 100 μm is chosen as a clad material. It is well known that, AISI 4140 steel is a typical candidate material for making a variety of cutting tools (dies and punches) and automotive parts. Mazumdar et al. (1997) and Choi and Hua (2004) reported that tool steel H13 exhibits an excellent combination of hardness and toughness at elevated temperatures. It has a huge potential of high volume usefulness for repairing the valued components and tools. The chemical composition of AISI 4140 (Jiang and Kovacevic, 2007) and H13 are summarized in Table 1. The tool steel H13 chemical composition is given by the manufacturer, Carpenter Powder Products Inc., PA.

Coupon preparation prior to laser cladding includes: (1) cutting the coupons by an abrasive water-jet machine (AWJ) at a size of 40 mm × 25 mm × 6 mm, (2) grinding the top surface of the coupon to remove the oxide layer, and (3) sand-blasting the top surface of the coupon by an aluminum oxide in a blasting chamber to increase the laser coupling efficiency by roughening the top surface of the coupon. (4) An advanced digital micro-hardness tester (Clark CM-700 AT) is used to measure the substrate hardness. A load of 200 gf for a dwelling time of 15 s is used for all the measurements. The measured value of the average surface hardness of the substrate is 258 kgf/mm^2.

The complete experimental setup of diode laser cladding is shown in Fig. 1a. The laser head is attached to the arm of a 6-axis industrial robot. The laser head is compact and easily mounted to the robot arm. The robot-controlled laser head is flexibly moved along non-uniform profile parts. A chiller is used to cool the laser head during laser cladding. Argon is used as a shielding gas to protect the optics of the laser head as well as to shield the laser–material interaction zone in order to prevent the oxidation of the molten material. The power control of the direct diode laser is integrated with a robot controller. A robot-controlled program is used to change the active state (on or off) of the laser, the laser power, scanning speed, and the time delay between successive tracks/layers.

The workstation includes the laser head, powder feeder nozzle, and machine vision system is shown in Fig. 1b. The machine vision system shown in Fig. 1b consists of the following components:

1. A CCD camera operating at a frame speed of 30 frames/s (fps) with a resolution of 404 × 315 pixels and a focal lens of 250 mm.
2. A 6-W continuous mode green laser with a wavelength of 532 nm is used as an illumination source.
3. A neutral density optical filter with a narrow-band pass filter of 532 nm ± 10 nm is used.

In Fig. 1b, the CCD camera and the green laser are fixed with the laser head at an equal distance in a mutually perpendicular plane at

Table 1
Chemical composition of the AISI 4140 and H13 (wt.%).

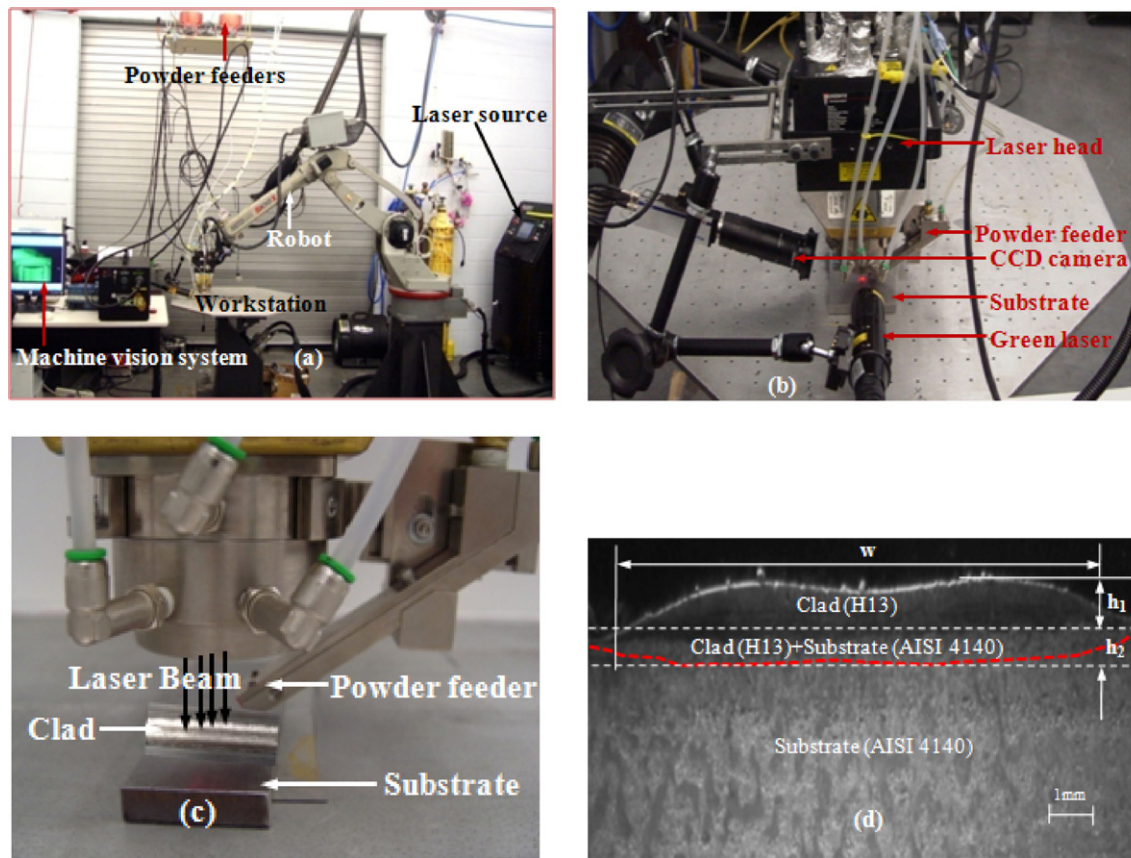| Materials	C	Cr	Mn	Mo	Si	S	P	V	Ni	Fe
AISI 4140	0.40	1.00	0.90	0.2	0.2	0.04	0.035	. . .	. . .	Balance
H13	0.41	5.35	0.35	1.40	1.00	0.03	0.03	0.90	0.30	Balance

Fig. 1. (a) Overall experimental setup for laser cladding process, (b) workstation, (c) off-axis powder injection system, and (d) cross-sectional micrograph (25×) of the cladded coupon.

an angle of 45° to the laser–material interaction zone. The CCD camera, the green laser, and the powder feeder operate simultaneously to determine the surface conditions at the laser–material interaction zone and the powder flow concentration at the nozzle outlet in real-time. The close view of an off-axis powder injection system installed with the laser head is shown in Fig. 1c. The cross-sectional micrograph of the diode laser clad is shown in Fig. 1d.

A 2-kW direct diode laser of 808 nm in wavelength with a rectangular-shaped laser spot of 12 mm × 1 mm and uniform distribution (top-hat) of laser power is used to carry out the experiments. An off-axis rectangular-shaped powder injection setup shown in Fig. 1c is used to feed the powder into the molten pool generated by the laser beam. Picasso et al. (1994) and Fathi et al. (2006) reported that the powder feed rate has a significant effect on the geometrical features (size, shape) of the clad. In this experimental setup, the powder feed rate is controlled by the regulation of powder feeder's motor speed. In order to determine uniform powder feeding across the length of laser spot (12 mm), a number of experiments are carried out by changing the motor speed from 200 rpm to 600 rpm. A double-sided tape is fixed on the plate to capture the powder for different motor speeds. The collected powders are weighed by a digital scale to determine the powder feed rate (g/s). The relationship between the powder feed rate vs. motor speed is shown in Fig. 2a. The machine vision system shown in Fig. 1b is used to

monitor the powder flow concentrations at the nozzle exit in real-time. The real-time image of the powder flow concentrations at the nozzle exit is shown in Fig. 2b. At the motor speed of 500 rpm, the powder feeder delivered uniform feeding of powder across the length of laser spot at a powder feed rate of 0.7 g/s. The laser power from 1400 W to 1800 W at an increment of 200 W, scanning speeds from 6 mm/s to 9 mm/s at 1 mm/s increments for a constant powder feed rate of 0.7 g/s are used to obtain different clad sizes.

The coupon preparation prior to post-cladding includes: (1) cutting the clad coupons by an AWJ machine to a size of 25 mm × 20 mm × 6 mm; (2) mounting the coupons in a cylindrical enclosure of 50 mm in radius and 6 mm in height made of a polyvinyl chloride (PVC) thermoset filled up with 9:1 proportion of the mixture of resin (RR 128) and hardener (RH 16); (3) gradually grinding the top and bottom surfaces of the mounted coupons using a lower feed rate to remove the oxides and make the coupon surfaces flat; (4) polishing the coupons on the Mark V Lab 3B/4B dual wheel machine by using a different GRIT of 120, 240, 400, 600, 800 and 1000 slicon carbide impedded papers in a plenty of water cleansing environment; (5) mirror polishing the coupons on the rotating velvet cloth disc by using an alumina powder paste of 1 μm and 0.05 μm; and (6) etching the coupons with 2% Nital followed by cleaning the coupons with alcohol for a standard metallographic procedure.
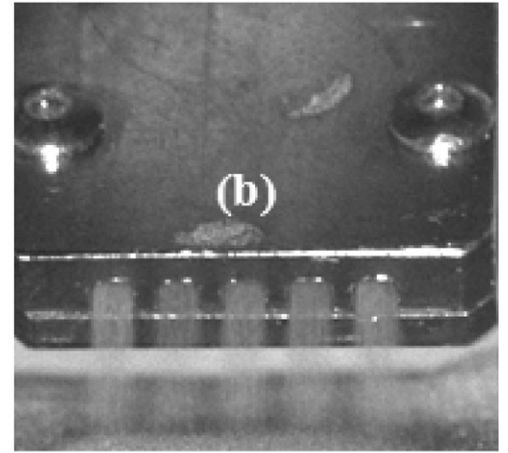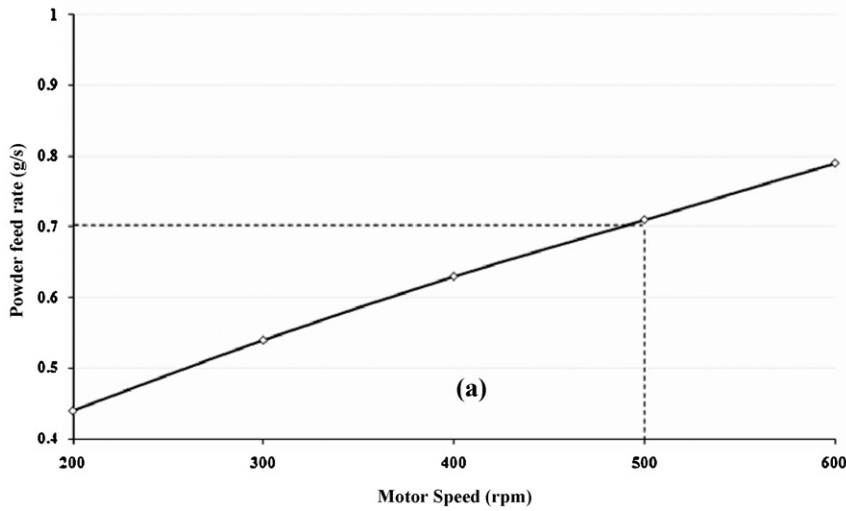
Fig. 2. . (a) Powder feed rate (g/s) vs. powder feeder motor speed (rpm), and (b) real-time powder flow image captured by a CCD camera.

Etched coupons micrographs are taken by an ultra high-resolution optical microscope (Keyence VHX-500 K). A cross-sectional micrograph at the magnification of 25× shown in Fig. 1d is used to measure the width (w), height (h_1) of the clad, and the dilution (h_2) of the clad material to the substrate. The optical micrographs at a magnification of 1000× are used to characterize the microstructure of the clad (H13) and the substrate (AISI 4140). The hardness below 25 μm at the top surface of the clad and across the clad to the substrate is measured by a digital micro-hardness tester (Clark CM-700 AT). A load of 200 gf and a dwelling time of 15 s are used to make an indentation on the measured spot. The Vickers hardness is automatically calculated based on the image of the diagonal length of the resulting permanent indentation taken by the camera fixed above the measured spot.

3. Finite element model (FEM) for laser cladding

In the laser cladding process, the temperature evolution across the cross section of the clad to the substrate is dependent on the process parameters. A finite element method (FEM) is used to solve the heat conduction equation shown in Eq. (1). From that result, the temperature history of the clad to the substrate can be predicted. The ANSYS (11.0) software with ANSYS Parametric Design Language (APDL) is used to generate a numerical code to predict the temperature history of the clad to the substrate for various processing parameters.

3.1. FEM assumptions and governing equation

In order to obtain reasonable accuracy and computational efficiency, the following assumptions are incorporated in the model:

1) The substrate (AISI 4140 steel) and the clad material (H13 tool steel) are isotropic, homogeneous, and temperature-dependent.
2) A constant direct diode laser efficiency, $\beta = 0.72$ (Nash et al., 2004) and absorptivity, $\eta = 0.75$ (Capello et al., 2007) are assumed.
3) The shrinkage allowance and material evaporation are neglected.
4) The molten pool free surface of the clad is assumed to be flat.

The 3-D transient heat conduction governing equation for a homogeneous, isotropic solid material without heat generation
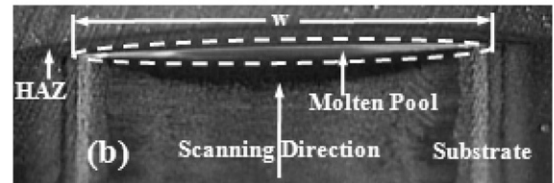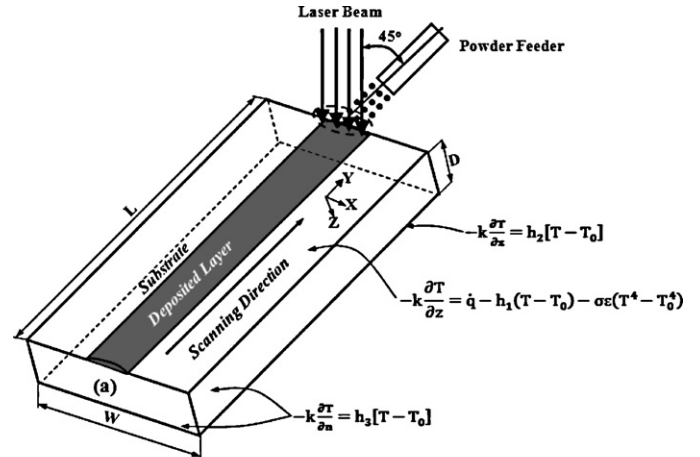

Fig. 3. (a) Schematic presentation of coupon geometry and the laser beam scanning direction and (b) real time molten pool image captured by a CCD camera.

using a Cartesian coordinate system (x, y, z) is described below:

$$\rho \frac{\partial(c(T)T)}{\partial t} = \frac{\partial^2}{\partial x^2}(k(T)T) + \frac{\partial^2}{\partial y^2}(k(T)T) + \frac{\partial^2}{\partial z^2}(k(T)T) \tag{1}$$

where, ρ is the density of material (kg/m³), $c(T)$ is the temperature-dependent specific heat (J/kg °C) and $k(T)$ is the temperature-dependent thermal conductivity of the material (W/m °C).

3.2. Coupon geometry

A schematic presentation of the cladded coupon with the coordinate system (x, y, z), scanning direction (y-axis), and the boundary conditions are shown in Fig. 3a. The real-time molten pool captured by the CCD camera is shown in Fig. 3b. This molten pool is used as a

reference for designing the shape of the heat source model shown in Eq. (4). The x-axis is referred to as the direction along the width (W) of the coupon, the z-axis is referred to as the direction across the cross section (D) of the coupon, and the y-axis is referred to as the scanning direction of the laser beam. A rectangular-shaped laser spot (12 mm × 1 mm) with uniform distribution (top-hat) of laser power is moving along the scanning direction (y-axis). This high power laser beam generates a constant heat flux ($\dot{q}$) that increases the temperature distribution across the cross section (z-axis) of the clad.

3.3. Initial and boundary conditions

In FEM, the numerical simulation of temperature distribution governed by Eq. (1) is subjected to the following initial and boundary conditions shown in Fig. 3a. At time, $t = 0$, the initial temperature of the coupon, $T_0 = 25\,°C$, and the initial state of the coupon are described below:

$$T(x, y, z) = T_0 \tag{2}$$

The heat generated by the laser beam is dissipated by convection to the boundary surfaces, and the radiation effect of the laser beam from the top surface of the coupon is shown in Eq. (3):

$$-k\frac{\partial T}{\partial z} = \dot{q} - h_1(T - T_0) - \sigma\varepsilon(T^4 - T_0^4) \tag{3}$$

In Eq. (3), the heat flux ($\dot{q}$) is applied perpendicular to the scanning direction of the laser beam, h_1 is the forced convection coefficient at the top surface (W/m^2 °C), T is the surface temperature (°C) of the coupon, T_0 is the room temperature (25 °C), σ is the Stefan Boltzmann constant (5.67×10^{-8} W/m^2 k^4), and ε (0.25) is emissivity of the surface (Capello et al., 2007).

The rectangular heat source model (Nash et al., 2004) having uniform (top-hat) distribution of laser power is described below:

$$\dot{q} = \begin{cases} \dfrac{\eta P}{w \times 1} & \text{for} \quad -\dfrac{w}{2} \leq x \leq \dfrac{w}{2}, \quad \text{and} \quad -\dfrac{1}{2} \leq z - \text{v.t} \leq 1/2 \\ 0 & \text{for others} \end{cases} \tag{4}$$

where, $P = \beta P_L$, β is the laser efficiency, η is the absorption coefficient, P_L is the laser power (W), w is the laser spot width (12 mm) along the x-axis of the coupon, and l is the laser spot length (1 mm) along the y-axis of the coupon.

Laser efficiency (β) can be defined as the ratio of the measured laser power by the energy meter to the actual power delivered by the laser. A coherent energy meter, Power Max (PM) 10 K, is used to measure the power delivered by HPDDL. Six-sets of readings shown in Table 2 are recorded by using different levels of laser power. The average efficiency is found to be 71.64%.
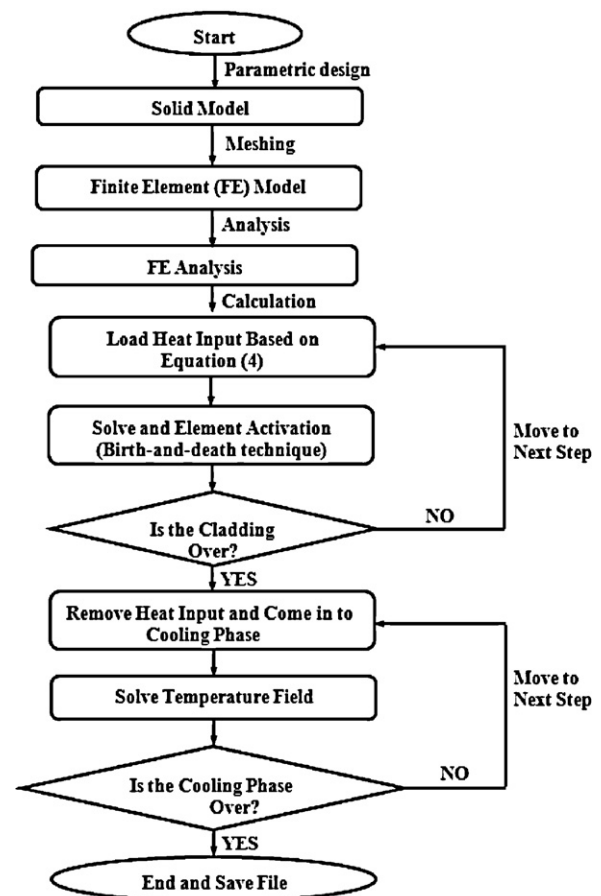

Fig. 4. Flow chart of the FEM procedure for thermal analysis.

The convection at the bottom surface of the coupon is shown in Eq. (5):

$$-k\frac{\partial T}{\partial z} = h_2(T - T_0) \tag{5}$$

where, h_2 is the equivalent convection coefficient at the bottom surface (W/m^2 °C). Here, the heat loss by conduction between the coupon and the work-plate is considered in the thermal analysis.

The other surface boundary conditions are described by Eq. (6):

$$-k\frac{\partial T}{\partial n} = h_3(T - T_0) \tag{6}$$

where, $k(\partial T/\partial n)$ denotes the surface temperature gradient along the normal direction n, h_3 is the natural convection coefficient (W/m^2 °C), and T is the surface temperature (°C).

Table 2
Efficiency measurement of the HPDDL.

Actual power (W)	Measured power (W)						Average (W)	Percentage (%)
	Trail 1	Trail 2	Trail 3	Trail 4	Trail 5	Trail 6		
1000	621	624	622	619	625	620	621.8	62.18
1100	695	692	697	694	691	696	694.1	63.10
1200	791	789	792	790	793	791	791	65.91
1300	862	865	863	864	861	860	862.5	66.34
1400	977	975	979	980	976	975	977	69.78
1500	1089	1092	1090	1092	1091	1090	1090.6	72.71
1600	1199	1196	1197	1195	1198	1196	1196.8	74.80
1700	1285	1283	1286	1281	1282	1283	1283.3	75.49
1800	1398	1395	1394	1391	1392	1390	1393.3	77.40
1900	1520	1517	1519	1518	1523	1520	1519.5	79.97
2000	1604	1610	1606	1612	1605	1608	1607.5	80.37
Average efficiency (%)								71.64

Table 3
Temperature-dependent thermal properties of AISI 4140 and H13 tool steel (Pinkerton and Li, 2004; Wen and Shin, 2009; Woo and Cho, 1999).

Temperature (°C)	Specific heat (J/kg °C)		Thermal conductivity (W/m °C)	
	AISI 4140	H13	AISI 4140	H13
25	473	447	42.7	28.6
100	485	453	43.2	29.5
200	496	467	43.61	30.29
300	512	484	45.31	31.99
400	529	502	47.01	33.69
500	541	519	48.71	35.39
600	556	537	50.41	37.09
700	579	554	52.11	38.79
800	594	572	53.81	40.49
900	619	589	55.51	42.19
1000	635	607	57.21	43.89
1100	664	625	58.91	45.59
1200	682	642	60.61	47.29
1300	703	660	62.31	48.99
1400	726	677	64.01	50.69
1500	747	692	31	19.06
1600	764	708	33.08	21.98
1700	781	721	35.64	24.06
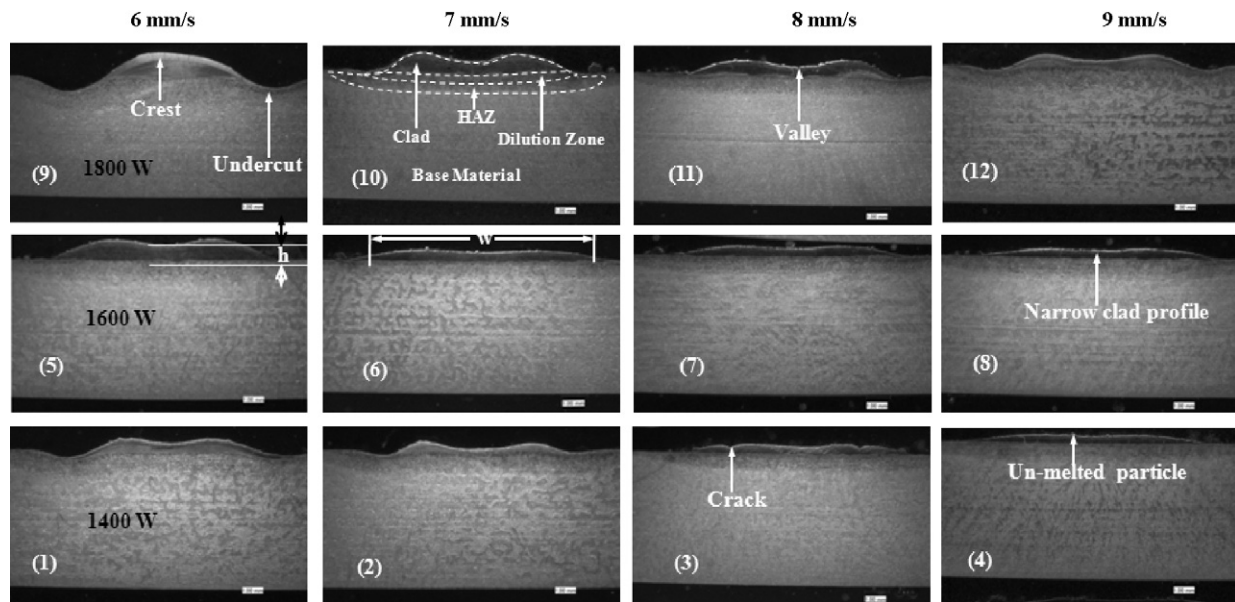
Fig. 5. Cross-sectional micrographs (25×) of the cladded coupon under various processing parameters.

3.4. Material properties and numerical procedures

In this model, a quadratic, cube-shaped element (SOLID 70) with eight nodes is used to discrete the coupon's geometrical domain. The uniform grid sizes of 0.025 mm for the clad and 0.05 mm for other surfaces are used to generate finer meshed coupon in 3-D. The temperature-dependent materials properties and phase change kinetics are adopted in this model. The temperature-dependent materials properties of AISI 4140 (Foroozmer and Kovacevic, 2009) and H13 (Pinkerton and Li, 2004) are summarized in Table 3.

The initial and boundary conditions shown in Eqs. (2) through (6) are used for the FE analysis. The heat transfer coefficients for forced convection (h_1), equivalent convection (h_2), and natural convection (h_3) are assumed to be: 180 W/m^2 °C (Woo and Cho, 1999), 100 W/m^2 °C, and 20 W/m^2 °C (Capello et al., 2007), respectively. A birth-and-death technique available in ANSYS is used to simulate the additive nature of the cladding process (Foroozmer and Kovacevic, 2009). Initially, all the elements in the clad regions are deactivated and subsequently activated as the heat source moves along the scanning direction (y-axis). The FE analysis is carried out

through a number of small time steps (Δt) with the time increment of 0.001 s. A number of iterations are performed to achieve a convergence criterion of 1% (the nodal temperature difference between two successive iterations). The procedure of the FE thermal model is shown in Fig. 4.

4. Results and discussion

4.1. Effect of processing parameters on the variation of clad geometry

In this study, the experiments are designed based on changing the laser power (1400–1800 W) and scanning speed (6–9 mm/s) while keeping the powder feed rate constant (0.7 g/s) to observe the variation in clad sizes. The cross-sectional micrographs of the cladded coupons for various processing parameters are shown in Fig. 5. In Fig. 5, the top row of micrographs denoted by 9–12 showed that crests, valleys, and undercuts are present in the clad. These defects could be due to the high heat input defined as a product of laser power and interaction time, i.e., the ratio between the

Table 4
Simulation matrix of cladding process parameters and results.

Ex. no	Laser power (W)	Scanning speed (mm/s)	Max. temp (°C)	Clad height (mm)	Dilution (mm)	Clad profile
1	1400	6	1693	0.53	0.23	NU → C, UC
2	1400	7	1641	0.47	0.20	NU → V
3	1400	8	1576	0.40	0.18	NU → V, Cr
4	1400	9	1525	0.28	0.15	NU → V, UC
5	1600	6	1784	0.87	0.35	NU → C
6	1600	7	1729	0.56	0.29	U
7	1600	8	1652	0.41	0.24	NU → N
8	1600	9	1576	0.32	0.20	NU → N, Cr
9	1800	6	1826	1.18	0.61	NU → V, UC
10	1800	7	1774	0.81	0.42	NU → C, Cr
11	1800	8	1709	0.62	0.32	NU → N, Cr
12	1800	9	1652	0.49	0.26	NU → N, UC

NU – non-uniform, U – uniform, C – crest, UC – undercut, V – valley, Cr – crack, and N – narrow.

scanning length of the laser beam over the substrate and the scanning speed. In addition, at the higher laser power, a nonuniform power distribution at the center of clad is observed. At the lower laser power, micrographs denoted by 1–4 in Fig. 5, show some cracks, unmelted particles, and uneven material deposition across the width of the clad. The cracked/broken clad occurs due to insufficient melting of the powder particles as well as the substrate (Adak et al., 2005). A narrow profile of the clad denoted by 7 and 8 in Fig. 5 could be caused by lower interaction time of the laser-powder and the substrate. A fairly uniform cladding process without undercuts and valleys denoted by 6 in Fig. 5 is achieved by the balanced heat input and cooling rate. It can be concluded that, the wavy nature of the free form (clad) surfaces decrease while the given heat input is in decrease (see micrographs denoted by 9–12 in Fig. 5). The free from surface tends to become narrow for a lower values of heat input (see micrographs denoted by 1–4 in Fig. 5). Hence, the free form surfaces (clad) obey the Marangoni flow (Picasso et al., 1994; Fathi et al., 2006).

The micrographs shown in Fig. 5 at the magnification of 25× are used to measure the clad height and dilution of the deposited material to the substrate. The clad sizes for various processing parameters are summarized in Table 4. The results show that for a specific powder feed rate (0.7 g/s), the clad height increases by
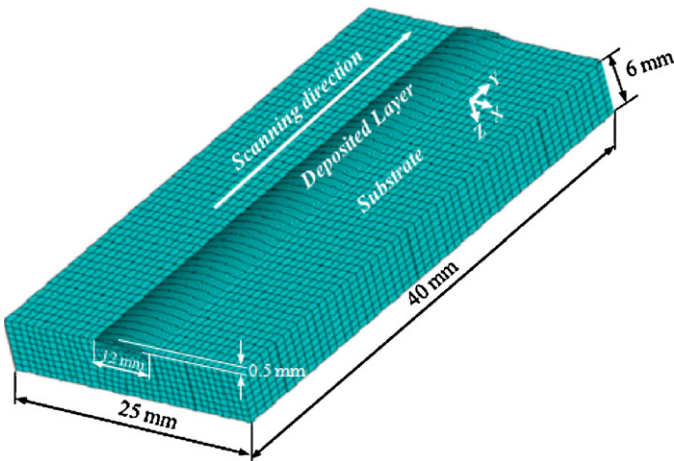

Fig. 6. The finite element meshed model of the coupon.

the decrease in scanning speed. The decrease in clad height by the increase in scanning speed is related to the interaction time of the laser beam with the powder and the substrate. Therefore, at a higher scanning speed less powder is deposited into the molten
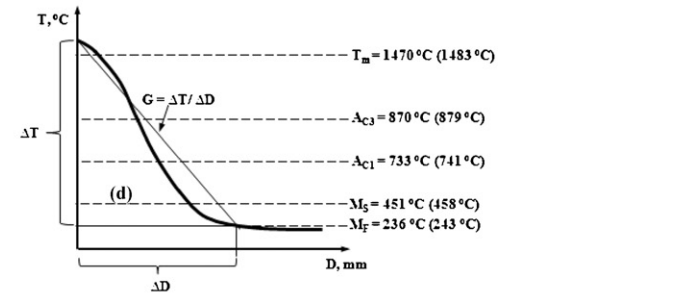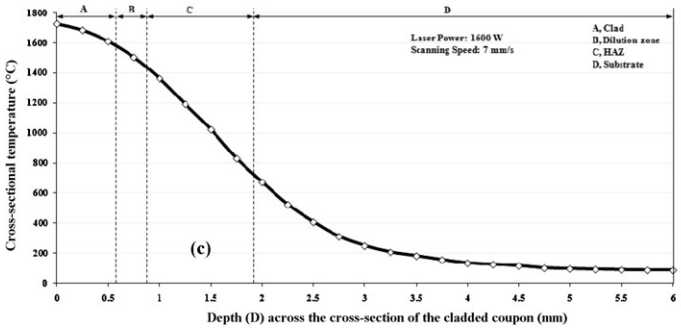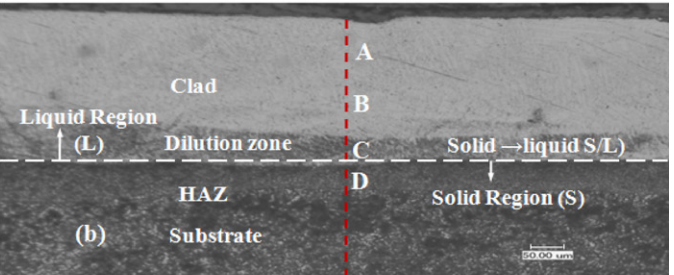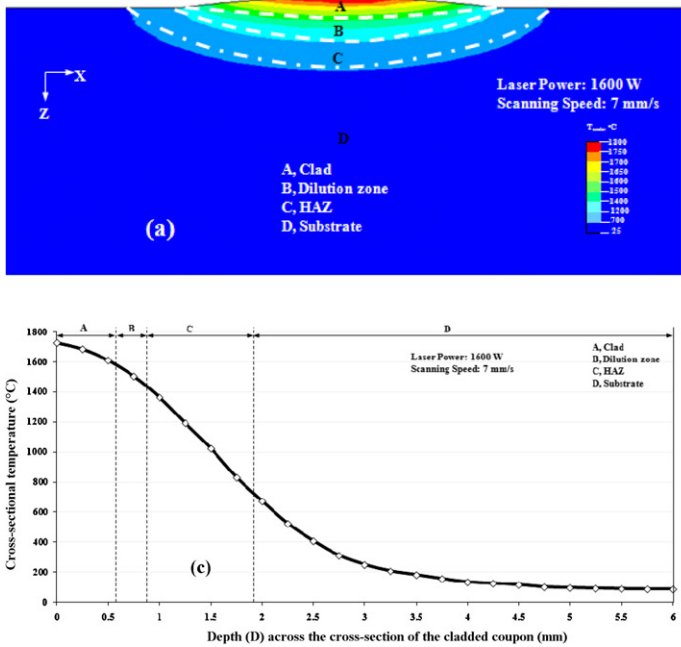

Fig. 7. (a) Modeled isotherms across the cross section of the cladded coupon (b) micrograph (300×) of the cladded coupon including, a clad, dilution zone, HAZ and substrate (c) cross-sectional temperature distribution, and (d) schematic presentation of temperature gradient (G) calculation.

pool. At a lower scanning speed, the clad height is relatively high as a result of the higher powder deposition into the molten pool due to a longer interaction time.

4.2. Prediction of temperature history and microstructure based on the rate of solidification during the laser cladding process

In the laser cladding process, the prediction of temperature history across the clad to the substrate is very important to calculate the heating rate (ε_{HR}), cooling rate ε_{CR}, temperature gradient (G), rate of solidification ($R = \varepsilon/G$) and the corresponding hardness (HV) (Picasso et al., 1994; Costa et al., 2005). The FE analysis for various processing parameters is carried out on the FE meshed coupon shown in Fig. 6 to predict the temperature history of the cladding process with respect to time and location. The finite elements defined in the mesh are updated over every time-step (Δt) for the continuous scanning of the laser beam over the substrate in order to describe the additive nature of the cladding process (Foroozmer and Kovacevic, 2009). The isotherms of the cladding process obtained from the FE thermal model at the laser power of 1600 W, and the scanning speed of 7 mm/s is shown in Fig. 7a. The isotherms shown in Fig. 7a compared with the micrograph (300×) shown in Fig. 7b, clearly show a clad, dilution zone, HAZ, and the substrate. The predicted maximum temperature and the measured clad height (h_1) and dilution (h_2) of the clad material to the substrate for various processing parameters are summarized in Table 4.

The temperature distribution from the top surface of the clad to the substrate is shown in Fig. 7c. In Fig. 7c, the maximum temperature at the top surface of the clad is about 1729 °C, which is 246 °C higher than the melting temperature, 1483 °C (Choi and Hua, 2004) of the clad material (H13) and 259 °C higher than the melting temperature, 1470 °C (Chiang and Chen, 2005) of the substrate (AISI 4140). At the higher temperature (1729 °C), the clad material and the top surface of the substrate are fully melted. A gradual decrease in temperature is observed in the dilution zone. In contrast, a sharp decrease in temperature is obtained in the HAZ to the substrate. The temperature distribution (T) across the cross section of the clad to the substrate is a function, $T = f(P, v, d)$ of the processing parameters, such as laser power (P) and scanning speed (v), and the distance (d) from the laser–material interaction zone to the substrate shown by an arrow in Fig. 8a (Fathi et al., 2006).

The temperature distribution (T) along the cross section (D) of the clad to the substrate shown in Fig. 7c is used to calculate the temperature gradient (G). The calculation procedure of temperature gradient is schematically shown in Fig. 7d. The temperature gradient, $G = \Delta T/\Delta D$ (°C/mm) is defined as the ratio of the temperature difference (ΔT) between the maximum temperature T (°C) at each location and the transformation temperature ($A_{C1}/A_{C3}/M_S/M_F$, °C), to the incremental depth (ΔD) (Kou, 2003). The transformation temperatures (A_{C1}, A_{C3}, M_S and M_F) play an important role to design the TK cycle during the cladding process. The empirical relationships available in the literatures are used to calculate transformation temperatures such as A_{C1} and A_{C3}, (Kasatkin and Vinokur, 1984), M_S (Li et al., 1998), and M_F (Hojerslev, 2001) temperatures of the AISI 4140 steel and H13. Here, A_{C1}, A_{C3}, M_S, and M_F are the temperatures (°C), representing the beginning of austenization, completion of austenization, beginning of the martensite phase, and completion of the martensite phase, respectively. The calculated A_{C1}, A_{C3}, M_S, and M_F temperatures of AISI 4140 and H13 are shown in Fig. 7d. The A_{C1}, A_{C3}, M_S, and M_F temperatures values of H13 are shown inside the brackets.

The temperature prediction locations (denoted by 1–13) from the top surface of the clad (0 mm) to the substrate up to 3 mm at 0.25 mm increments are schematically shown in Fig. 8a. The temperature across the clad to the substrate obtained from the FE thermal model at the locations denoted by 1–13 in Fig. 8a is shown
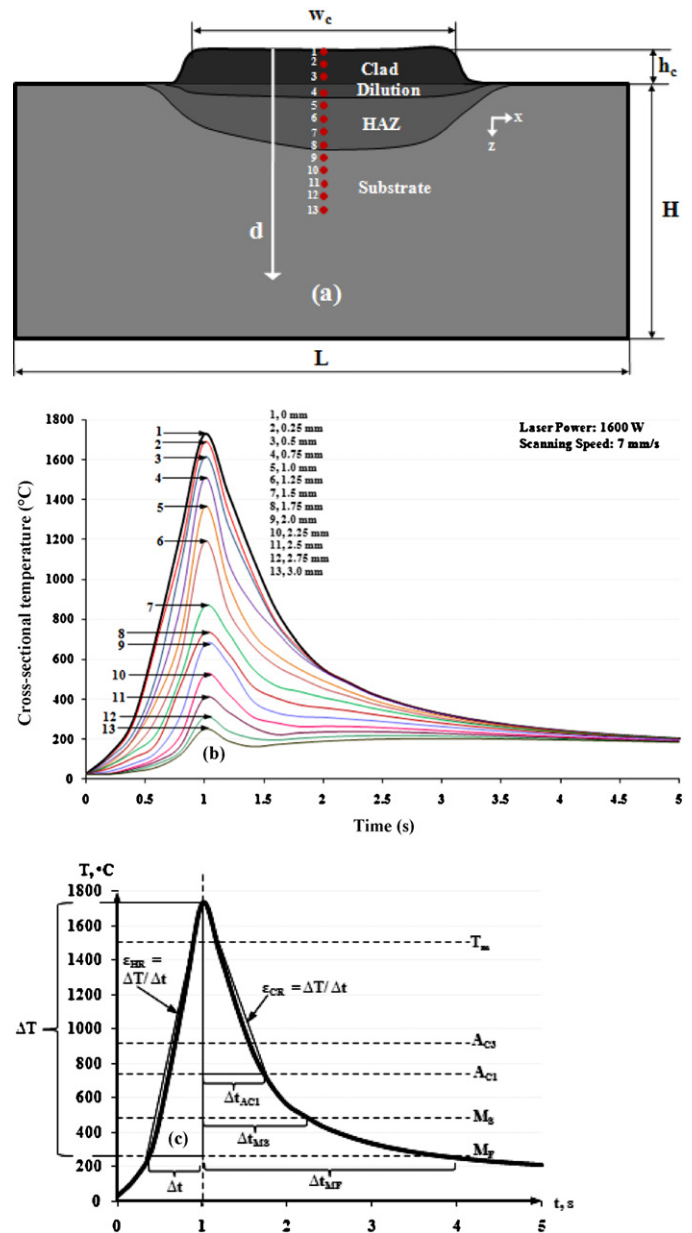

Fig. 8. (a) The temperature measured locations, (b) modeled cross-sectional temperatures with respect to time, and (c) schematic presentation of heating and cooling rates (ε) calculation.

in Fig. 8b. In Fig. 8b, three modes of austenization are achieved due to the variation in transformation temperatures ($A_{C1} \rightarrow A_{C3}$, and T_m). A rapid melting and solidification is achieved in the clad up to the dilution zone. A partial-austenization is achieved below the dilution zone and in the HAZ. A tempering effect due to the heating is achieved below the HAZ to the substrate.

The thermal cycles denoted by 1–13, shown in Fig. 8b are used to calculate the maximum heating and cooling rates from the top surface of the clad to the substrate. The heating/cooling rate, $\varepsilon = \Delta T/\Delta t$ (°C/s) is defined as the ratio of the temperature difference (ΔT) between the maximum temperature T (°C) at each location, and the transformation temperature ($A_{C1}/A_{C3}/M_S/M_F$, °C), for the time (s) increment (ΔT) (Kou, 2003). The calculation procedure of the heating and cooling rates is schematically illustrated in Fig. 8c for various transformation temperatures with respect to the change in time. In this case, the M_F temperature is chosen as a final transformation temperature of the cladding process to calculate the heating
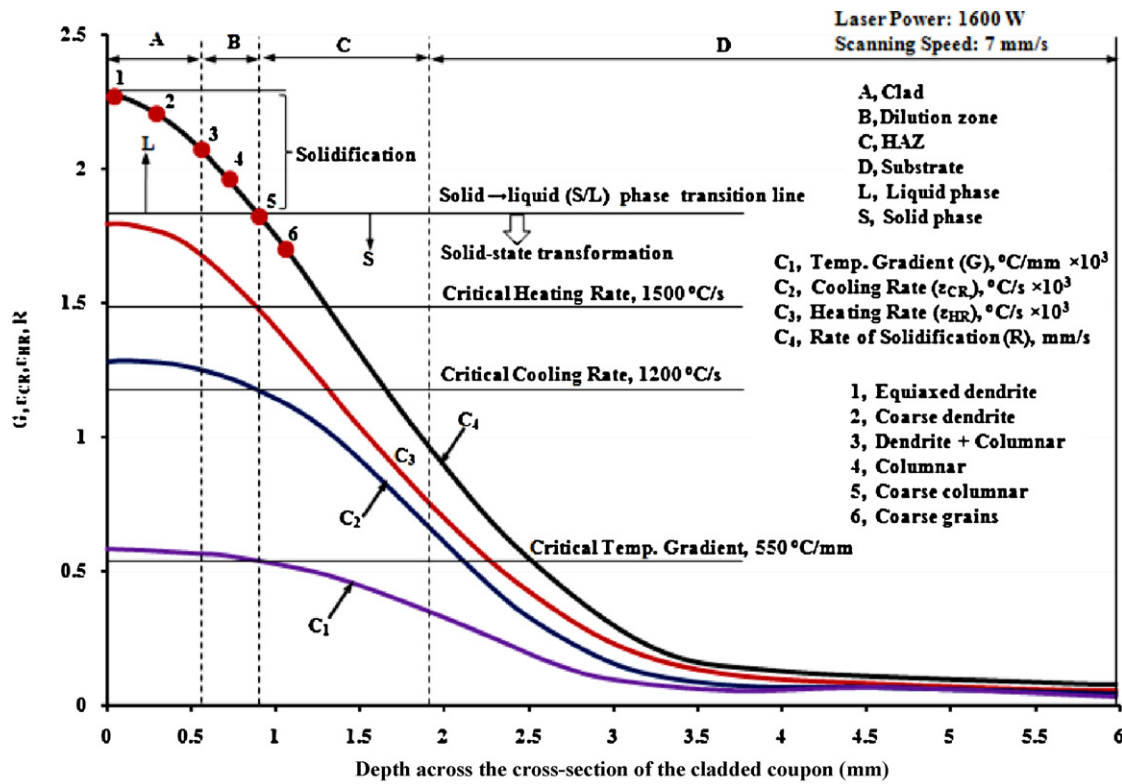
Fig. 9. Modeled temperature gradient (G), heating rate (ε_{HR}), cooling rate (ε_{cR}), and the rate of solidification/grain growth (R) with respect to the change in depth (D) of the cladded coupon.

and cooling rates. The rate of solidification (R, mm/s) is an important characteristic to predict the microstructure evolution during the cladding process. The rate of solidification, $R = \varepsilon/G$, (mm/s) is defined as the ratio between the cooling rate (ε, °C/s) and the temperature gradient (G, °C/mm) (Kou, 2003).

The predicted values of the temperature gradient, heating rate, and cooling rate, and the rate of solidification across the cross section of the cladded coupon at the laser power of 1600 W and scanning speed of 7 mm/s are denoted by the curves C_1 to C_4 shown in Fig. 9. A higher average of the values of the temperature gradient (575 °C/mm), heating rate (1725 °C/s), cooling rate (1300 °C/s), and the rate of solidification (2.2 mm/s) are achieved in the clad marked as A shown in Fig. 9. In the dilution zone, marked as B in Fig. 9, the average values of the temperature gradient, heating rate, cooling rate, and the rate of solidification are: 560 °C/mm, 1575 °C/s, 1225 °C/s, and 1.95 mm/s, respectively. In the HAZ, marked as C in Fig. 9, a sharp decrease in the temperature gradient (550 → 350 °C/mm), heating rate (1500 → 700 °C/s), cooling rate (1200 → 650 °C/s), and the rate of grain growth (1.8 → 0.95 mm/s) are achieved. The higher magnification (1000×) micrographs shown in Fig. 10 are taken at the locations A–D shown in Fig. 7b. The locations 1–6 marked in the micrographs shown in Fig. 10a–d and the points 1–6 marked in the curve C_4 in Fig. 9 are used to quantify the effect of the microstructure variation with respect to the change in the rate of solidification/grain growth in the liquid, the solid–liquid interface, and the solid regions of the cladding process. To compare the micrographs shown in Fig. 10a–d, and the numerical results shown in Fig. 9, a phase transition from solid-state to solidification is observed at the values of the temperature gradient of 550 °C/mm, heating rate of 1500 °C/s, cooling rate of 1200 °C/s, and at the rate of solidification of 1.8 mm/s.

The higher magnification (1000×) micrographs shown in Fig. 10 are categorized into four structures; dendrite, a mixture of dendrite and cellular, cellular, and coarse grains from the top of the clad

to the substrate. In Fig. 10a, near the top of the clad (location 1), a fine dendrite microstructure is present due to a higher rate of solidification by a higher temperature gradient and cooling rate. Whereas, at the bottom of the clad (location 2), a coarse dendrite structure is present. It can be seen that, the dendrite structure is solidified with different orientations. At the top of the clad, the dendrite structure appears like an epitaxial growth. At the center and bottom of the clad, the dendrite structure grows perpendicular to the laser scanning direction.

In Fig. 10b, a coarse dendrite structure is present at the top of the clad. A mixture of dendrite and columnar structure (location 3) is present from the middle to the bottom of the clad. The orientation of the columnar structure is followed by the previous orientation of the dendrite structure. In Fig. 10c, a columnar structure (location 4) is present at the bottom of the clad. A coarse columnar structure (location 5) is present at the dilution zone. The microstructure is predominantly cellular with an average grain size of 15 μm. In Fig. 10d, a coarse columnar structure (location 5) is present in the dilution zone and a mixture of coarse grains (location 6) is present in the HAZ.

4.3. Hardness calculation based on thermo-kinetic (TK) model

The hardness across the cross section of the cladded coupon is measured by a digital micro-hardness tester. The hardness measurement pattern is shown in Fig. 11. A load of 200 gf and a dwelling time of 15 s are used for all the measurements. The kinetic equation originally developed by Reti et al. (1987) shown in Eq. (7) is coupled with the FE thermal model to calculate the change in hardness.

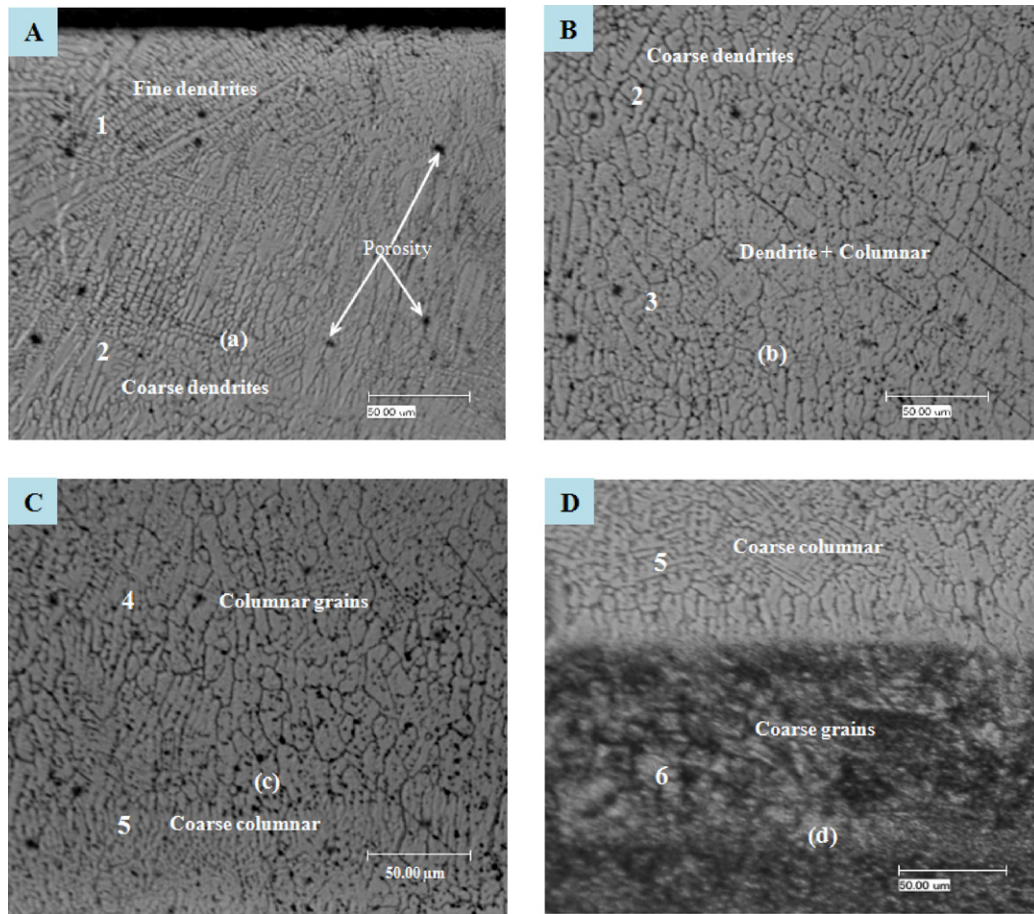$$HV_F = HV_I - A \left[\int_0^t \exp\left(\frac{Q}{RT(t)}\right) dt \right]^m \tag{7}$$

Fig. 10. Micrographs (1000×) of the cladded coupon (a) top of the clad, (b) intermediate area of the clad, (c) intermediate clad and dilution zone, and (d) the dilution zone, HAZ and substrate.
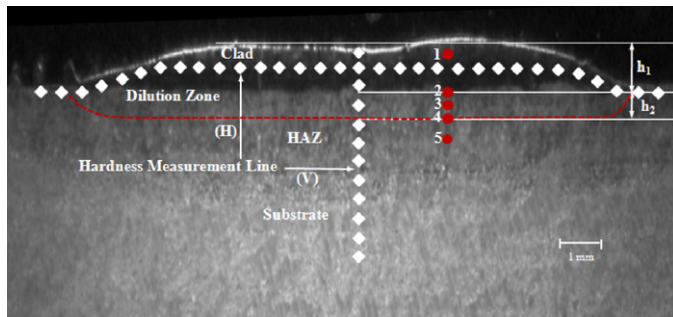

Fig. 11. Schematic presentation of hardness measurement on micrograph (25×) of the cladded coupon.

where, HV_F is the final hardness (kgf/mm^2), and HV_I is the initial hardness (kgf/mm^2). An additive rule is used to describe the percentage of clad material and the substrate material involved in the clad and in the dilution zone to determine the initial hardness. In Fig. 11, h_1 and h_2 are the height of the clad and the dilution of the clad material to the substrate, respectively. Based on the experimental trials of hardness measurement at the locations denoted by 1–5 shown in Fig. 11, the following combinations of percentage of the clad material and the substrate material are assumed to calculate the initial hardness: 100% H13, 80% H13 + 20% 4140, 50% H13 + 50% 4140, 20% H13 + 80% 4140, and 100% H13, respectively (Fathi et al., 2006). In Eq. (7), Q is the activation energy (kJ/mol), R is the gas constant (8.314472, J/°C mol), T is the instantaneous

temperature (°C), t is the time (s), and A and m are the material constants (Costa et al., 2005).

The activation energy with respect to change in temperature is calculated by solving the following differential equation (Li et al., 1998):

$$\frac{d}{dT}(\Delta T^n \exp^{(Q/RT)}) = 0 \tag{8}$$

which leads to the following relationship:

$$Q_{max} = \frac{nRT^2}{\Delta T} \tag{9}$$

The interpolated material-dependent constants, A and m for AISI 4140 steel and tool steel H13 are: 1375 HV/s and 0.3437, respectively (Costa et al., 2005). The substrate material (AISI 4140 steel) and the clad material (H13) hardness are: 258 HV (Celik and Ersozlu, 2009), and 240 HV (Lee et al., 2009), respectively. The cross sectional temperature distribution obtained from the FE thermal model shown in Fig. 8b and the values of HV_I, Q, A, and m are plugged in Eq. (7) to calculate the change in hardness.

The measured and modeled hardness distributions across the cross section of the cladded coupon are shown in Fig. 12. In the clad (0 → 0.56 mm) denoted by A in Fig. 12, the hardness varies from 671 HV to 649 HV. A higher average hardness of about 660 HV is achieved in the clad. This higher hardness is due to refinement of the fine dendrite structure shown in Fig. 10a by a higher average cooling rate of 1300 °C/s. In the dilution zone (0.56 mm → 0.85 mm) denoted by B in Fig. 12, the hardness decreases from 649 HV to 615 HV, as the result of the coarse dendrite structure, shown in
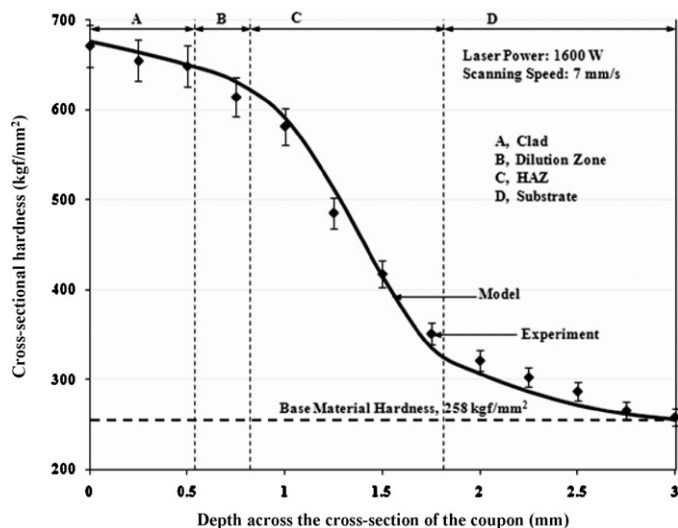
Fig. 12. Modeled and measured cross-sectional hardness distributions along the hardness measurement line marked as (*V*) shown in Fig. 11.
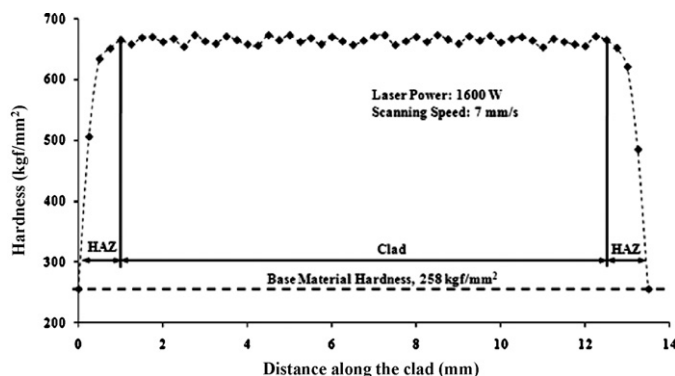

Fig. 13. Uniformity hardness measurements along the hardness measurement line marked as (*H*) shown in Fig. 11.

Fig. 10c and d. In the HAZ (0.85 mm → 1.8 mm), denoted by C in Fig. 12, the hardness decreases further from 615 HV to 320 HV. This steeper hardness variation could be a result of the presence of coarse grains shown in Fig. 10d. However, a fairly high hardness (615 HV) is achieved near the dilution zone. At a distance greater than 1.8 mm, denoted by D in Fig. 12, is the substrate that is not highly affected by the heat. Below the HAZ up to 3 mm towards substrate, a lesser variation (320 HV to 258 HV) in hardness is present. Below 3 mm, the substrate is not affected by the laser melting, and hardness has a steady value of about 258 HV.

The hardness along the clad is measured by a digital microhardness tester with the same loading and dwelling time as used for measuring hardness across the clad. The hardness measurement is done along the line denoted by H in Fig. 11 placed 250 μm from the top surface of the clad. For every measurement point along the line denoted by H in Fig. 11, two more measurements of hardness are taken, one at 100 μm above and the other one at 100 μm below the line denoted by H in Fig. 11, and the average value of these three measurements is taken as a final value of hardness. The measured average hardness values are shown in Fig. 13. The trend of the change of hardness shows its fairly uniform hardness distribution along the clad. At the edge of the clad is HAZ; therefore, a larger variation in hardness is achieved.

5. Conclusions

A defect-free and a good metallurgically bonded clad of tool steel H13 on the substrate of AISI 4140 steel of hardness uniformity is achieved by using a 2-kW HPDDL of 808 nm in wavelength. A FE thermal model incorporated the temperature-dependent material properties, phase change kinetics, and as-used experimental boundary conditions is developed to predict the temperature history, rates of heating and cooling cycles, temperature gradient, and the rate of solidification of the clad to the substrate. The FE thermal model coupled with TK equations is used to predict the change of hardness of the clad to the substrate. The hardness measurement and microstructure characterization are performed to evaluate the effect of processing parameters on the variation of clad geometry, microstructure, and the change of hardness. The predicted results show a good agreement with experimental ones in the as-used experimental boundary conditions, laser power, and scanning speed while keeping a constant powder feed rate. The microstructure study shows that four different zones are present across the clad: (1) a fine dendrite structure is present near the top surface of the clad; (2) a mixed dendrite and cellular structure are present in the intermediate clad; (3) followed by a cellular and coarse cellular structure in the dilution zone, and (4) coarse grains are present in the HAZ. Further, the coupled FE TK model can be used to predict the variation of microstructure and the change hardness of the clad to the substrate for any given process parameters.

Acknowledgements

References

Abe, N., Tukamoto, M., Fukuhara, S., Morimoto, J., 2004. Surface modification of TiO$_2$–ZiO$_2$ layers with direct diode laser. Transactions of JWRI 33 (2), 123–126.

Adak, B., Nash, P., Chen, D., 2005. Microstructural characterization of laser cladding of Cu–30Ni. Journal of Materials Science 40, 2051–2054.

Bonek, M., Dobrzanski, L.A., 2006. Functional properties of laser modified surface of tool steel. Journal of Achievements in Materials and Manufacturing Engineering 17 (1–2), 313–316.

Capello, E., Castrelnuovo, M., Previtali, B., Vedali, M., 2007. Surface treatment of welded duplex stainless steels by diode laser. Journal of Laser Applications 19 (3), 133–140.

Celik, S., Ersozlu, I., 2009. Investigation of the mechanical properties and microstructure of friction joints between AISI 4140 and AISI 1050 steels. Materials and Design 30, 970–976.

Chiang, K.A., Chen, Y.C., 2005. Laser surface hardening of H13 steel in the melt case. Materials Letters 59, 1919–1923.

Choi, J., Hua, Y., 2004. Dimensional and material characteristics of direct deposited H13 tool steel by CO$_2$ laser. Journal of Laser Applications 16 (4), 245–251.

Cook, C.M., Haake, J.M., Zediker, M.S., Banaskavich, 2000. Diode laser cladding produces high quality coatings. International SAMPE Technical Conference 32, 910–921.

Costa, L., Vilar, R., Reti, T., Deus, A.M., 2005. Rapid tooling by laser powder deposition: process simulation using finite element analysis. Acta Materialia 53, 3987–3999.

Fathi, A.L., Toyserkani, E., Khajepour, A., Durali, M., 2006. Prediction of melt pool depth and dilution in laser powder deposition. Journal of Physics D: Applied Physics 39, 2613–2623.

Foroozmer, E., Lin, D., Kovacevic, R., 2009. Application of vibration in the laser powder deposition process. Journal of Manufacturing Processes 11, 38–44.

Foroozmer, E., Kovacevic, R., 2009. Thermokinetic modeling of phase transformation in the laser powder deposition process. Metallurgical and Materials Transactions A 40A, 1935–1943.

Han, L., Liou, F.W., Phatak, K.M., 2004. Modeling of laser cladding with powder injection. Metallurgical and Materials Transactions B 35B, 1139–1150.

Hojerslev, C., 2001. Tool Ssteels. RISO National Laboratory, Roskilde.

Huang, Y.L., Liu, J., Ma, N.H., Li, J.G., 2006. Three-dimensional analytical model on laser-powder interaction during laser cladding. Journal of Laser Applications 18 (1), 42–46.

Jiang, W.H., Kovacevic, R., 2007. Laser deposited TiC/H13 tool steel composite coatings and their erosion resistance. Journal of Materials Processing Technology 186, 331–338.

Kasatkin, O.G., Vinokur, B.B., 1984. Calculation models for determining the critical points of steel. Metal Science and Heat Treatment 26 (1–2), 27–31.

Kinkade, K., 2006. Diode lasers test their mettle in surface treatment. Laser Focus World, 95–97.

Kou, S., 2003. Welding Metallurgy. Wiley-Interscience, pp. 145–242.

Lawrence, J., 2006. A high power diode laser-based technique for the bonding of composite patches of aluminum alloys on various military aircraft. Journal of Laser Applications 18 (2), 151–155.

Lee, J.H., Jang, J.H., Joo, B.D., Son, Y.M., Moon, Y.H., 2009. Laser surface hardening of AISI H13 tool steel. Transactions of Nonferrous Metals Society of China 19, 917–920.

Li, M.V., Niebuir, D.V., Meekiho, L.L., Atteridge, D.G., 1998. A computational model for the prediction of steel hardenability. Metallurgical and Materials Transactions B, 661–672.

Mazumdar, J., Choi, J., Nagarathnam, K., Koch, J., Hetzner, D., 1997. The direct metal deposition of H13 tool steel for 3-D components. Journal of Operations Management, 55–60.

Nash, P., Hu, Z., Zhou, G., Adak, B., 2004.Molten pool size in laser cladding simulated by finite element method. Materials Science & Technology (MS&T'04), pp. 303–311.

Nowotny, S., Richter, A., Beyer, E., 1998. Laser cladding using high-power diode lasers. International Congress on Applications of Lasers & Electro-Optics (ICALEO'98), pp. G68–G74.

Ouyang, J.H., Mei, H., Valant, M., Kovacevic, R., 2002. Application of laser-based additive manufacturing to production of tools for friction stir welding. Solid Freeform Fabrication Proceedings, 65–72.

Picasso, M., Marsden, C.F., Wagniere, J.D., Frenk, A., Rappaz, M., 1994. A simple but realistic model for laser cladding. Metallurgical and Materials Transactions B 25B, 281–291.

Pinkerton, A.J., Li, L., 2004. Modeling the geometry of a moving laser melt pool and deposition track via energy and mass balances. Journal of Physics D: Applied Physics 37, 1885–1895.

Reti, T., Gergely, M., Tardy, P., 1987. Mathematical treatment of non-isothermal transformations. Materials Science and Technology 3 (5), 365–371.

Syed, W.U.H., Pinkerton, A.J., Li, L., 2005. A comparative study of wire feeding and powder feeding in direct diode laser deposition for rapid prototyping. Applied Surface Science 247, 268–276.

Uenishi, K., Ogata, Y., Iwatani, S., Adachi, A., Sato, T., Kobayashi, K.F., 2007. Laser cladding of Fe–Cu based alloys on aluminum. Solid State Phenomena 127, 331–336.

Wen, S., Shin, Y.C., 2009. Modeling of the off-axis high power diode laser (HPDL) cladding process. In: Proceedings of the ASME 2009 International Manufacturing Science and Engineering Conference (MSEC 2009), Paper#: MSEC2009-84049, pp. 1–10.

Woo, H.G., Cho, H.S., 1999. Three-dimensional temperature distribution in laser surface hardening processes. Proceedings of the Institution of Mechanical Engineers (IMechE) Part B: Journal of Engineering Manufacture 213, 695–712.

Technical specifications, 2009. Carpenter powder products Inc., Bridgeville, PA. www.cartech.com (accessed November 2009).